## APPLIED PHYSICS

# Octave-spanning tunable infrared parametric oscillators in nanophotonics

Luis Ledezma[1,2], Arkadev Roy[1], Luis Costa[1], Ryoto Sekine[1], Robert Gray[1], Qiushi Guo[1], Rajveer Nehra[1], Ryan M. Briggs[2], Alireza Marandi[1]*

**Widely tunable coherent sources are desirable in nanophotonics for a multitude of applications ranging from communications to sensing. The mid-infrared spectral region (wavelengths beyond 2 μm) is particularly important for applications relying on molecular spectroscopy. Among tunable sources, optical parametric oscillators typically offer some of the broadest tuning ranges; however, their implementations in nanophotonics have been limited to narrow tuning ranges in the infrared or to visible wavelengths. Here, we surpass these limits in dispersion-engineered periodically poled lithium niobate nanophotonics and demonstrate ultrawidely tunable optical parametric oscillators. Using 100 ns pulses near 1 μm, we generate output wavelengths tunable from 1.53 μm to 3.25 μm in a single chip with output powers as high as tens of milliwatts. Our results represent the first octave-spanning tunable source in nanophotonics extending into the mid-infrared, which can be useful for numerous integrated photonic applications.**

## INTRODUCTION

Widely tunable coherent sources are vital for applications ranging from multichannel optical communications (1) to LiDAR (2). Wide tunability in the mid-infrared spectral range is especially desirable because of the rich molecular responses at wavelengths longer than 2 μm (3). While it is possible to generate light at these wavelengths with semiconductor lasers (4), the tuning ranges are typically narrow because of limited bandwidth of semiconductor gain (5–8). Alternatively, optical parametric oscillators (OPOs) based on quadratic nonlinearity have been a prominent example of sources with flexible and broad tuning ranges, which have commonly been realized using nonlinear crystals in bulky tabletop setups (9).

Previous efforts toward OPO miniaturization include using lithium niobate–diffused waveguides with fiber feedback loops (10), semiconductor waveguides with Bragg mirrors deposited on the chip end facets (11), and whispering-gallery microresonators (12, 13). However, implementation of OPOs in nanophotonics with subwavelength modal confinement and low propagation losses is highly desirable because of opportunities for dense integration with other on-chip components, strong nonlinear interactions, and dispersion engineering (14).

Over the past decade, nanophotonic OPOs were demonstrated in the near-infrared and visible ranges using materials with cubic [$\chi^{(3)}$] and quadratic [$\chi^{(2)}$] nonlinearities (15–22). However, the main advantages of tabletop OPOs, namely, wide tunability and mid-infrared coverage, have not yet been accessed in nanophotonics. A noteworthy roadblock for this is the typical use of simple pump resonant configurations in which all the interacting optical fields resonate simultaneously in a single resonator. This leads to ultralow OPO thresholds at the expense of an overconstrained wavelength tunability. In contrast, OPOs with singly or doubly resonant configurations (i.e., with nonresonant pump) offer wide tunability and frequency stability (9).

Here, we design and demonstrate ultrawidely tunable doubly resonant OPOs in lithium niobate nanophotonics. This is achieved by combining dispersion engineering, precise design of the spectral response of the cavity, and quasi-phase matching. With a pump tunable over 30 nm at around 1 μm, we achieve wavelengths tunable from 1.53 to 3.25 μm from five OPOs on a single nanophotonic chip.

## RESULTS

The tuning concept of the OPOs is illustrated in Fig. 1A, where more than 1500 nm of tuning around 2 μm for the signal and idler is obtained by tuning the pump wavelength around 1 μm by less than 30 nm. Such a tuning range for the pump is already available from integrated distributed Bragg reflector (DBR) semiconductor lasers (23). Such magnification in tuning range from the pump toward the signal and idler (a factor of ~12 in frequency units) is obtained through a dispersion-engineered quasi-phase–matched OPO design with a spectrally selective cavity as depicted in Fig. 1B. We use wavelength-selective couplers that allow the signal and idler wavelengths to resonate in the OPO cavity with a ~10 GHz free spectral range (FSR) while letting the pump go only through the poled waveguide section (24). This differs sharply from previously demonstrated fully resonant on-chip OPO designs in which the pump also needs to satisfy a resonant condition limiting their flexibility and tunability. A chip containing 16 OPOs is fabricated, as shown in Fig. 1C, where we have highlighted a single OPO, which is also displayed in the false color optical microscope image of Fig. 1D.

The simulated tuning behavior of four OPOs with different poling periods is shown in Fig. 1E (solid black lines). These are obtained from conservation of energy ($\omega_p = \omega_s + \omega_i$) and momentum ($k_p = k_s + k_i + 2\pi/\Lambda_{\text{QPM}}$), so they can be tailored by engineering the waveguide dispersion (25). In particular, the signal tuning slope ($\partial\omega_s/\partial\omega_p$) is given by the ratio of group velocity differences ($1/v_i - 1/v_p$)/($1/v_i - 1/v_s$), while the gain bandwidth is inversely proportional to $1/v_i - 1/v_s$. We have engineered the dispersion of the poled

[1]Department of Electrical Engineering, California Institute of Technology, Pasadena, CA 91125, USA. [2]Jet Propulsion Laboratory, California Institute of Technology, Pasadena, CA 91109, USA.
*Corresponding author. Email: marandi@caltech.edu
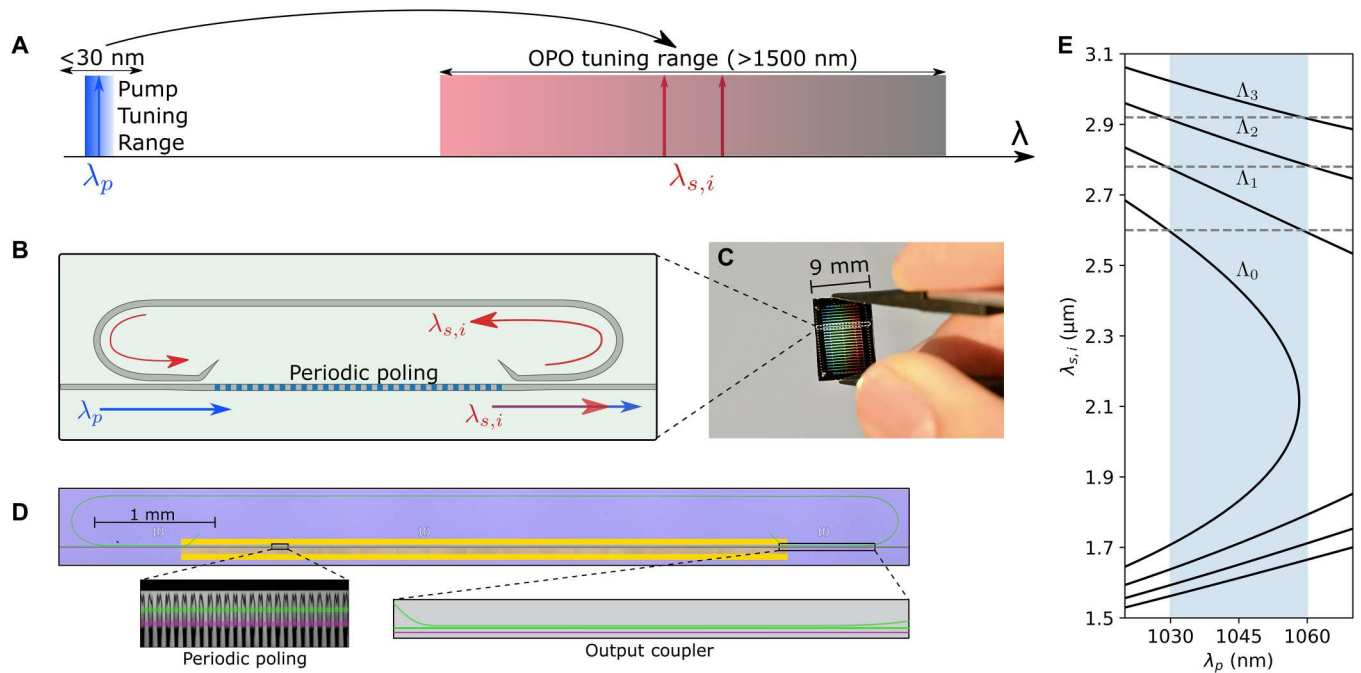
**Fig. 1. Ultrawidely tunable OPOs in nanophotonics.** (**A**) A narrowly tunable (<30 nm) pump around 1 μm leads to an OPO signal and idler tuning range exceeding 1500 nm. (**B**) Schematic of the doubly resonant parametric oscillator with a frequency-selective resonator that provides feedback only to the signal and idler while enabling continuous tuning of the pump. (**C**) Image of the chip highlighting the area occupied by a single OPO. (**D**) False color optical microscope image of the OPO (green) and a straight waveguide (purple, used for calibration and phase-matching verification). Insets show a two-photon microscope image of the periodic poling and a close-up of the adiabatic output coupler. (**E**) Example of OPO tuning curves for four different poling periods Λ0 to Λ3. The dashed vertical lines and the blue stripe are to guide the eyes on how continuous tuning over an octave can be achieved with four poling periods and only 30 nm of pump tuning.

waveguide to balance these effects. As a result, a small change in the pump wavelength produces large changes in the output wavelengths while maintaining a predictable tuning curve without substantial mode competition (see fig. S1).

To study the transient and steady-state behaviors of the nanophotonic OPOs, we use pulses that are much longer than the cavity lifetime of the OPOs. This arrangement also allows us to use low average powers incident on the chip while maintaining high peak powers. The experimental setup is shown in Fig. 2A, which is described in detail in Materials and Methods.

The measured OPO on-chip signal power at ~1950 nm is shown in Fig. 2B as a function of on-chip pump power (at 1050 nm). Only the signal (red squares) is measured, as the photodetector is not sensitive to the idler wave near 2275 nm. The idler power (purple circles) is estimated from the output coupler response (see Materials and Methods). The solid black line is a fit based on a theoretical expression with an oscillation threshold of ~30 mW (30 μW of average power). Figure 2C shows the on-chip conversion efficiency, which has a maximum value of ~9% for the signal and up to ~15% when including the idler. This efficiency is limited by the escape efficiency of the OPO (see Materials and Methods), which is currently low for the idler, and can be enhanced substantially with different coupler designs. Pump depletion characterizes the efficiency with which pump photons are converted into signal and idler photons inside the OPO (see Materials and Methods). As shown in Fig. 2D, ~75% is observed, highlighting the potential of nanophotonic OPOs as extremely efficient wavelength conversion devices. These

large pump depletion levels are also readily apparent from the oscilloscope traces shown in Fig. 2 (E and F).

Figure 3 shows the spectral tuning range of five OPOs fabricated on the same chip. Figure 3 (top) shows few spectra of the signal and idler emission of the OPOs. This includes an OPO (OPO1, red traces) that can operate at degeneracy (top trace), and an OPO (OPO5, orange traces) that can achieve signal and idler wavelengths separated by more than an octave, and with an idler wavelength well into the mid-infrared.

More spectra from the same OPOs are shown in Fig. 3 (middle), demonstrating dense coverage over the entire spectral range, except for a band around ~2.8 μm where the SiO$_2$ buffer layer exhibits an absorption peak (*26*). The tuning parameter in all these cases was the pump wavelength as illustrated in the vertical axis of the bottom panel. Note that OPO1 can be tuned between 1.76 and 2.51 μm (over 750 nm) by varying the pump wavelength by only 30 nm, corresponding to a tuning magnification factor of ~12 in frequency units. OPO1 can also operate at degeneracy by using a 1060 nm pump, as shown in the topmost trace of the top panel, corresponding to the black dot in the bottom panel.

By tuning the pump power level, the OPOs can operate with a single mode, few modes, or multiple mode clusters, with examples shown in Fig. 4. Closer to threshold, the OPOs can oscillate in a single spectral mode, as shown in Fig. 4A. As the pump power is increased, oscillation in a few modes can occur, as shown in Fig. 4B. Multiple mode clusters appear several times above threshold, as shown in Fig. 4C. The multimode behavior is due to the parametric gain bandwidth being larger than 1 THz, so a large number
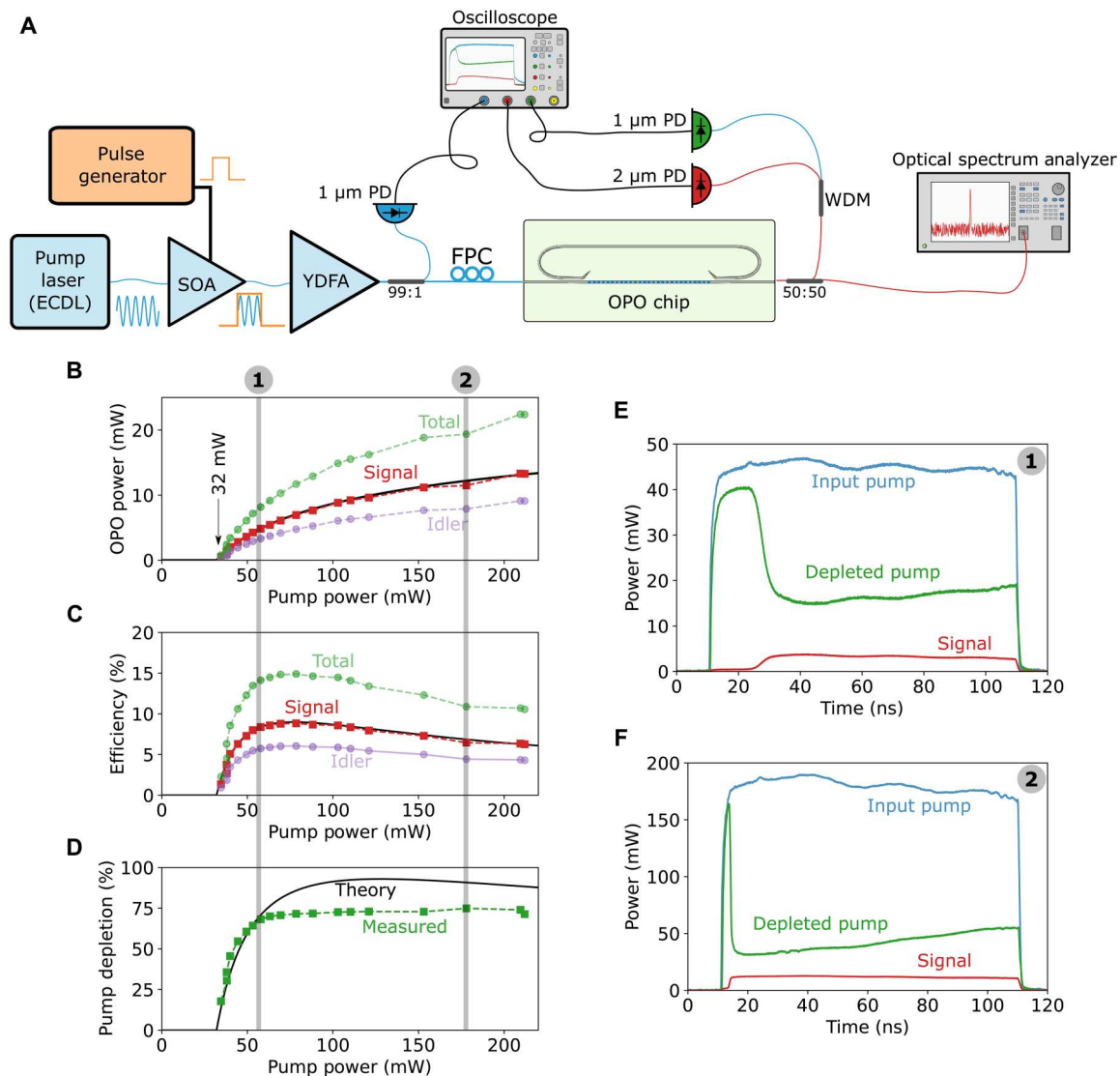
**Fig. 2. Transient and steady-state measurements of on-chip doubly resonant OPOs.** (**A**) Measurement setup. We use 100 ns pulses with a 10 kHz repetition rate to decrease the average power while keeping the peak power above the OPO threshold. ECDL, external cavity diode laser; SOA, semiconductor optical amplifier; YDFA, ytterbium doped fiber amplifier; FPC, fiber polarization controller; OPO, optical parametric oscillator; PD, photodetector; WDM, wavelength division multiplexer. (**B**) On-chip output power versus pump power for a signal wavelength of 1950 nm and a pump wavelength of 1050 nm; the idler and total power are estimated from the signal (see Materials and Methods). (**C**) Different measured on-chip efficiencies. (**D**) Measured and expected pump depletion levels representing the conversion efficiency within the OPO. (**E** and **F**) Measured pump and signal traces at two different power levels, as indicated by the shaded gray regions in (B) to (D).

of modes (~10 GHz FSR) experience gain. At the same time, waveguide dispersion causes a difference in FSR between signal and idler wavelengths, which produces cluster effects in doubly resonant OPOs well above threshold (*27*). Further dispersion and cavity engineering can be used for either suppressing the multimode effects or tailoring it toward generation of frequency combs (*28*).

Figure 5 shows the tuning range and peak power level of our OPO chip in the quasi–continuous wave (CW) regime alongside previously reported tunable sources in nanophotonics, which operate in the CW regime. Such notable performance is enabled by our nonresonant pump OPO design combined with dispersion-engineered, quasi-phase–matched, directly etched waveguides (see Materials and Methods).

## DISCUSSION

Our results show that ultrawidely tunable infrared sources can be implemented on the thin-film lithium niobate platform, adding to the increasingly large set of functionalities available in this platform (*29*) and complementing the recent demonstration of tunable near-infrared DBR lasers (*23*). The threshold and required pump tuning range of our OPOs are within the reach of low-cost near-infrared laser diodes. Additional engineering of the cavity design, waveguide dispersion, and quasi-phase matching can be used for tailoring the operation toward a multitude of applications. For instance, the threshold of the OPOs can be substantially reduced by using a separate resonator for the pump without sacrificing the conversion efficiency and tunability (unlike a triply resonant design).
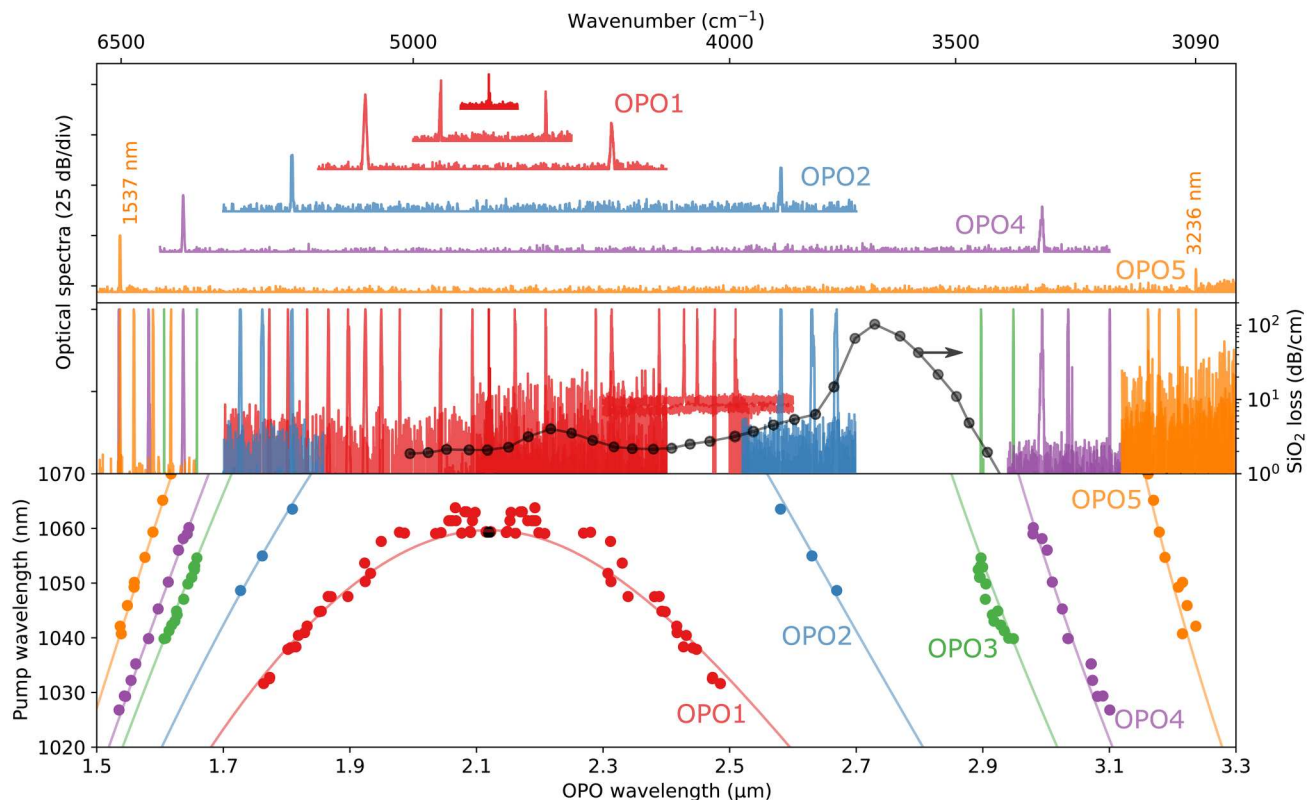
**Fig. 3. Wavelength tuning of nanophotonic OPOs.** (**Top**) Examples of output spectra for a few OPOs on the same chip exhibiting an octave-wide tuning range. Each color represents a different OPO. (**Middle**) Many more output spectra from the same OPOs. (**Bottom**) All measured data (colored dots) with the corresponding pump wavelength on the vertical axes along with the theoretical tuning curves (solid lines).

The maximum conversion efficiency of a doubly resonant OPO is dominated by its escape efficiency, which is related to the ratio of output coupler transmittance to total resonator losses (see Materials and Methods). For our device, this ratio is ~9% at 1950 nm, indicating that the output coupling is small compared to the total losses in the resonator. This could be caused in part by the little transmission of the output coupler, particularly at mid-infrared wavelengths, and in part by intrinsic resonator losses and losses at the input coupler. Fine tuning of the coupler designs and reducing the cavity loss can lead to substantial improvement of efficiency. We used adiabatic couplers in this work since they provide a simple means to approximately achieve our requirements of high signal and idler coupling together with low pump coupling. However, the input coupler should, ideally, have 100% coupling at signal and idler frequencies since any transmission in this coupler behaves as additional resonator loss, leading to higher thresholds and lower efficiencies.

Simultaneously, the input coupler should provide very low coupling at the pump wavelength, since any coupling just leaks pump power into the unused port, and also provides an undesired feedback path for the pump. These characteristics may be achievable through more advanced coupler designs, for instance, those obtained by inverse design methods (30).

The tuning range of a single OPO can be further enhanced by implementing multiple poling periods on the same OPO. Moreover, since the wavelength coverage of the OPO appears to be limited by the loss of the SiO$_2$ buffer layer, a similar design with a different buffer layer material can allow operation toward the entire lithium niobate transparency window (31). The OPO design we demonstrate here can also be readily applied to other emerging nonlinear photonic platforms with transparency windows deeper into the mid-infrared (32).

The measurements presented in Fig. 3 only exploit the dependence of the output wavelength on pump wavelength. Two additional degrees of freedom are the temperature and the resonator's FSR (which could be varied, for instance, by electro-optic modulation of the resonator's feedback arm). These three variables combined can facilitate precise and fast tuning of the output wavelengths over a much broader spectral range (26), especially when an integrated pump laser is used.

Singly resonant OPOs offer even smoother tunability and stability characteristics at the expense of higher threshold powers. While pure singly resonant behavior can be obtained by changing the coupler response so that only the signal or idler resonates, we note that the transition between doubly and singly resonant designs is smooth (33) and we have evidence that our OPOs can operate in this regime (see fig. S2). This could enable fast and ultrabroad wavelength synthesis on-chip with potential mode-hop free operation.

In summary, we have demonstrated on-chip doubly resonant OPOs that can be tuned over an octave up to 3.25 μm. Our OPOs are based on an innovative on-chip doubly resonant design that avoids many of the challenges present in triply resonant configurations and linear cavity oscillators, and can be easily extended to singly resonant configurations. Further dispersion engineering
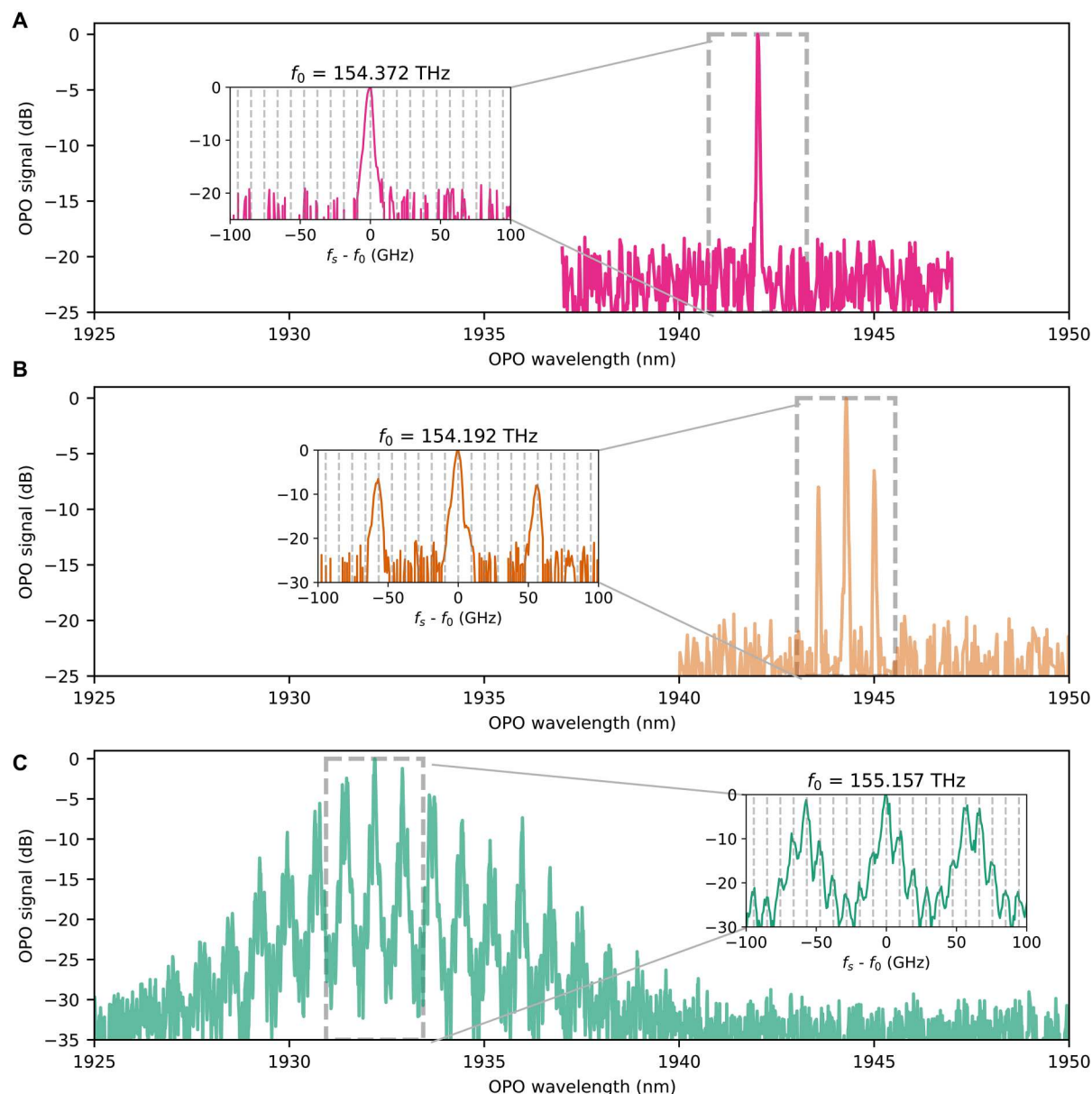
**Fig. 4. Spectral structures of free-running OPOs.** The generated spectrum of our OPOs can vary from (**A**) single-mode emission, to (**B**) emission in a few modes separated by several FSRs, to (**C**) emission in several mode clusters. Insets show close-up of spectra with dashed vertical lines separated by the resonator's FSR, which is approximately equal to the 10 GHz OSA resolution bandwidth.

may lead to femtosecond synchronously pumped OPOs in nanophotonics and the numerous applications they unlock (*34*).

## MATERIALS AND METHODS
### Device design
We use adiabatic couplers to create the wavelength selective cavity (see fig. S1A). The input and output couplers are identical and are designed so that signal and idler wavelengths ($\lambda > 1.8$ μm) have large coupling factors (>80%), while pump wavelengths near 1 μm are only slightly coupled (<10%). The residual coupling of the pump leads to round-trip feedback factors of less than 1% that produce

negligible modulations of the pump intensity as a function of frequency, allowing continuous tuning of the pump wavelength.

When designing a tunable OPO, it is desirable to have a large tuning slope so a small change in pump wavelength produces large changes in the output wavelengths. At the same time, a small gain bandwidth is preferable to limit the number of resonator modes experiencing gain. To achieve a balance between these two behaviors, we engineer the dispersion of the waveguide using its geometry, resulting in 2.5-μm-wide waveguides on a 700-nm-thick lithium niobate layer and 250 nm of etching depth. The mode profile for a set of representative wavelengths is shown in fig. S1B, illustrating that the modal overlap remains substantial despite the large frequency difference.
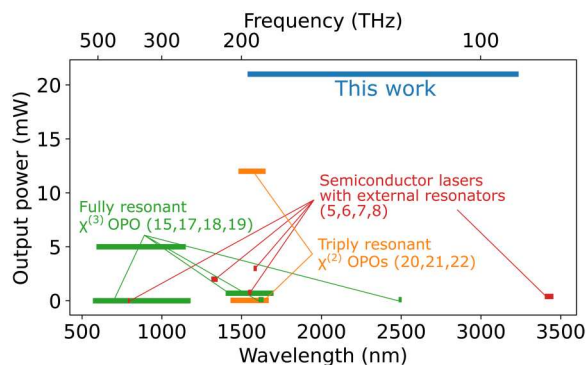
**Fig. 5. Comparison of the on-chip output power and wavelength coverage of our on-chip OPOs with other integrated tunable sources.** The power level is the sum of signal and idler for all OPOs.

## Device fabrication

We fabricate our devices using a commercial wafer (NANOLN) with an x-cut, 700-nm-thick MgO-doped lithium niobate layer and a $SiO_2$ buffer layer. We provide quasi-phase matching in a 5-mm-long region through periodic poling (inset of Fig. 1B shows a second-harmonic microscope image of a typical poled section). The waveguides are patterned by e-beam lithography and dry etched with $Ar^+$ plasma to a depth of 250 nm. All the OPOs have the same waveguide geometry obtained from dispersion engineering, with 2.3-μm-wide input and output waveguides that taper (through the adiabatic couplers) to 2.5-μm-wide waveguides inside the resonator. To maximize the spectral range covered on a single chip, we fabricated OPOs with poling periods ranging from 5.55 to 5.7 μm in 10-nm steps. We include a straight waveguide next to each OPO for calibration and quasi-phase matching verification (colored purple in Fig. 1B).

## Device characterization

We characterize our OPOs using the experimental setup shown in Fig. 2A, which consists of a tunable CW 1 μm laser amplified by a semiconductor optical amplifier, which is modulated to generate 100-ns-long (full-width-half-maximum) pulses with 10-kHz repetition rate. These pulses are further amplified by an ytterbium-doped fiber amplifier and coupled into the chip using a single-mode 1 μm lensed fiber (~10 dB coupling loss). The OPO output is collected by either a 2 μm lensed fiber or a cleaved InF3 fiber and sent to an optical spectrum analyzer (OSA) or to an InAsSb detector connected to an oscilloscope. A wavelength division multiplexer allows us to monitor the depleted pump and signal output simultaneously.

To estimate propagation losses in our waveguides, we fabricated chips with arrays of critically coupled resonators and extracted quality factors $\sim 6 \times 10^5$, which translate to losses below 0.3 dB/cm for waveguides without poling. Detailed inspection of the periodically poled waveguide inside the resonator reveals periodic roughness of the waveguide sidewalls, likely from the polarization-dependent etch rate of lithium niobate. More studies are needed to improve the resonator quality factor.

To estimate input and output coupling losses, we use single-mode lensed fibers to couple into and out of the chip and then divide the total throughput loss equally between both interfaces. We do this on several unpoled straight waveguides and obtain a

coupling coefficient varying from 10 to 13 dB, with 10 dB giving the most conservative estimate for on-chip input power. When using an asymmetric setup (lensed fiber at input, cleaved fiber at output), we assume that the input coupling remains at 10 dB and calculate the output coupling from the throughput loss. Comparing transmission of straight waveguides to that of OPOs allows us to estimate a total loss factor of 0.929 per coupler at the pump wavelength, reasonably close to the simulated value of 0.95 (fig. S1A). The plots of Fig. 2 (B to D) are obtained from oscilloscope traces like those in Fig. 2 (E and F) by first converting voltage to power, integrating them to find the energy, and then dividing them by the 100 ns pulse width to obtain the average peak power.

## Efficiency and idler power estimation

The efficiency of an OPO (η) can be written as the product of two efficiencies, $\eta = \eta_0 \eta_e$. The internal efficiency ($\eta_0$) measures how efficiently pump photons are converted into signal and idler photons, while the escape efficiency ($\eta_e$) measures the fraction of the generated signal and idler photons available at the output of the OPO. The difference between the pump power at the beginning and end of the gain section is $\Delta P_p = P_p(0) - P_p(L_g)$. The internal efficiency is just the pump depletion $\eta_0 = \Delta P_p/P_p(0)$ shown in Fig. 2D.

The escape efficiency is given by $\eta_e = (\omega/\omega_p) \, T(\omega)/[1 - L(\omega)]$, where $T(\omega)$ is the power transmission coefficient of the output coupler, while $L(\omega)$ is the total round-trip power loss factor of the resonator, i.e., $L(\omega) = [1 - T(\omega)]^2 \exp(-2\alpha L)$, where α is the field propagation loss, assumed constant, and the square term comes from considering identical input and output couplers. Since the output power can be calculated from the efficiency as $P_{\text{out}}(\omega) = \eta_0 \eta_e(\omega) P_p(0)$, the idler power can be estimated from the signal power and the simulated coupler response, $T(\omega)$, as

$$P_{\text{out}}(\omega_i) \approx \frac{\eta_e(\omega_i)}{\eta_e(\omega_s)} \, P_{\text{out}}(\omega_s) = \frac{\omega_i}{\omega_s} \frac{T(\omega_i)}{T(\omega_s)} \frac{1 - L(\omega_s)}{1 - L(\omega_i)}$$

## Supplementary Materials

**This PDF file includes:**
Figs. S1 and S2

## REFERENCES AND NOTES

1. A. E. Willner, *Optical Fiber Telecommunications VII* (Academic Press, 2020).
2. Y. Jiang, S. Karpf, B. Jalali, Time-stretch LiDAR as a spectrally scanned time-of-flight ranging camera. *Nat. Photonics* **14**, 14–18 (2020).
3. I. E. Gordon, L. S. Rothman, R. J. Hargreaves, R. Hashemi, E. V. Karlovets, F. M. Skinner, E. K. Conway, C. Hill, R. V. Kochanov, Y. Tan, P. Wcisło, A. A. Finenko, K. Nelson, P. F. Bernath, M. Birk, V. Boudon, A. Campargue, K. V. Chance, A. Coustenis, B. J. Drouin, J. -M. Flaud, R. R. Gamache, J. T. Hodges, D. Jacquemart, E. J. Mlawer, A. V. Nikitin, V. I. Perevalov, M. Rotger, J. Tennyson, G. C. Toon, H. Tran, V. G. Tyuterev, E. M. Adkins, A. Baker, A. Barbe, E. Canè, A. G. Császár, A. Dudaryonok, O. Egorov, A. J. Fleisher, H. Fleurbaey, A. Foltynowicz, T. Furtenbacher, J. J. Harrison, J. -M. Hartmann, V.-M. Horneman, X. Huang, T. Karman, J. Karns, S. Kassi, I. Kleiner, V. Kofman, F. Kwabia-Tchana, N. N. Lavrentieva, T. J. Lee, D. A. Long, A. A. Lukashevskaya, O. M. Lyulin, V. Y. Makhnev, W. Matt, S. T. Massie, M. Melosso, S. N. Mikhailenko, D. Mondelain, H. S. P. Müller, O. V. Naumenko, A. Perrin, O. L. Polyansky, E. Raddaoui, P. L. Raston, Z. D. Reed, M. Rey, C. Richard, R. Tóbiás, I. Sadiek, D. W. Schwenke, E. Starikova, K. Sung, F. Tamassia, S. A. Tashkun, J. V. Auwera, I. A. Vasilenko, A. A. Vigasin, G. L. Villanueva, B. Vispoel, G. Wagner, A. Yachmenev, S. N. Yurchenko, The HITRAN2020 molecular spectroscopic database. *J. Quant. Spectrosc. Radiat. Transf.* **277**, 107949 (2022).
4. Y. Yao, A. J. Hoffman, C. F. Gmachl, Mid-infrared quantum cascade lasers. *Nat. Photonics* **6**, 432–439 (2012).

5. E. Shim, A. Gil-Molina, O. Westreich, Y. Dikmelik, K. Lascola, A. L. Gaeta, M. Lipson, Tunable single-mode chip-scale mid-infrared laser. *Commun. Phys.* **4**, 268 (2021).

6. Y. Han, Y. Han, X. Zhang, X. Zhang, R. Ma, M. Xu, H. Tan, J. Liu, R. Wang, S. Yu, X. Cai, Widely tunable O-band lithium niobite/III-V transmitter. *Opt. Express* **30**, 35478–35485 (2022).

7. M. Li, L. Chang, L. Wu, J. Staffa, J. Ling, U. A. Javid, S. Xue, Y. He, R. Lopez-Rios, T. J. Morin, H. Wang, B. Shen, S. Zeng, L. Zhu, K. J. Vahala, J. E. Bowers, Q. Lin, Integrated pockels laser. *Nat. Commun.* **13**, 5344 (2022).

8. C. O. de Beeck, F. M. Mayor, S. Cuyvers, S. Poelman, J. F. Herrmann, O. Atalar, T. P. McKenna, B. Haq, W. Jiang, J. D. Witmer, G. Roelkens, A. H. Safavi-Naeini, R. V. Laer, B. Kuyken, III/V-on-lithium niobate amplifiers and lasers. *Optica* **8**, 1288–1289 (2021).

9. M. H. Dunn, M. Ebrahim-Zadeh, Parametric generation of tunable light from continuous wave to femtosecond pulses. *Science* **286**, 1513–1518 (1999).

10. C. Langrock, M. M. Fejer, Fiber-feedback continuous-wave and synchronously pumped singly-resonant ring optical parametric oscillators using reverse-proton-exchanged periodically-poled lithium niobate waveguides. *Opt. Lett.* **32**, 2263–2265 (2007).

11. M. Savanier, C. Ozanam, L. Lanco, X. Lafosse, A. Andronico, I. Favero, S. Ducci, G. Leo, Near-infrared optical parametric oscillator in a III-V semiconductor waveguide. *Appl. Phys. Lett.* **103**, 261105 (2013).

12. N. Amiune, D. N. Puzyrev, V. V. Pankratov, D. V. Skryabin, K. Buse, I. Breunig, Optical parametric-oscillation-based $\chi^{(2)}$ frequency comb in a lithium niobate microresonator. *Opt. Express* **29**, 41378–41387 (2021).

13. N. L. B. Sayson, T. Bi, V. Ng, H. Pham, L. S. Trainor, H. G. L. Schwefel, S. Coen, M. Erkintalo, S. G. Murdoch, Octave-spanning tunable parametric oscillation in crystalline Kerr micro-resonators. *Nat. Photonics* **13**, 701–706 (2019).

14. C. Wang, C. Langrock, A. Marandi, M. Jankowski, M. Zhang, B. Desiatov, M. M. Fejer, M. Loncar, Ultrahigh-efficiency wavelength conversion in nanophotonic periodically poled lithium niobate waveguides. *Optica* **5**, 1438–1441 (2018).

15. L. Razzari, D. Duchesne, M. Ferrera, R. Morandotti, S. Chu, B. E. Little, D. J. Moss, CMOS-compatible integrated optical hyper-parametric oscillator. *Nat. Photonics* **4**, 41–45 (2010).

16. X. Lu, G. Moille, A. Singh, Q. Li, D. A. Westly, A. Rao, S.-P. Yu, T. C. Briles, S. B. Papp, K. Srinivasan, Milliwatt-threshold visible–telecom optical parametric oscillation using silicon nanophotonics. *Optica* **6**, 1535–1541 (2019).

17. X. Lu, G. Moille, A. Rao, D. A. Westly, K. Srinivasan, On-chip optical parametric oscillation into the visible: Generating red, orange, yellow, and green from a near-infrared pump. *Optica* **7**, 1417–1425 (2020).

18. Y. Tang, Z. Gong, X. Liu, H. X. Tang, Widely separated optical Kerr parametric oscillation in AlN microrings. *Opt. Lett.* **45**, 1124–1127 (2020).

19. J. R. Stone, X. Lu, G. Moille, K. Srinivasan, Efficient chip-based optical parametric oscillators from 590 to 1150 nm. *APL Photonics* **7**, 121301 (2022).

20. A. W. Bruch, X. Liu, J. B. Surya, C.-L. Zou, H. X. Tang, On-chip $\chi^{(2)}$ microring optical parametric oscillator. *Optica* **6**, 1361–1366 (2019).

21. J. Lu, A. A. Sayem, Z. Gong, J. B. Surya, C.-L. Zou, H. X. Tang, Ultralow-threshold thin-film lithium niobate optical parametric oscillator. *Optica* **8**, 539–544 (2021).

22. T. P. McKenna, H. S. Stokowski, V. Ansari, J. Mishra, M. Jankowski, C. J. Sarabalis, J. F. Herrmann, C. Langrock, M. M. Fejer, A. H. Safavi-Naeini, Ultra-low-power second-order nonlinear optics on a chip. *Nat. Commun.* **13**, 4532 (2022).

23. P. A. Verrinder, L. Wang, J. Fridlander, F. Sang, V. Rosborough, M. Nickerson, G. Yang, M. Stephen, L. Coldren, J. Klamkin, Gallium arsenide photonic integrated circuit platform for tunable laser applications. *IEEE J. Sel.* **28**, 1–9 (2022).

24. A. Marandi, L. Ledezma, Y. Xu, R. M. Briggs, Thin-film optical parametric oscillators. U.S. Patent 11,226,538 (2022).

25. L. Ledezma, R. Sekine, Q. Guo, R. Nehra, S. Jahani, A. Marandi, Intense optical parametric amplification in dispersion-engineered nanophotonic lithium niobate waveguides. *Optica* **9**, 303–308 (2022).

26. R. A. Soref, S. J. Emelett, W. R. Buchwald, Silicon waveguided components for the longwave infrared region. *J. Optics A* **8**, 840–848 (2006).

27. R. C. Eckardt, C. D. Nabors, W. J. Kozlovsky, R. L. Byer, Optical parametric oscillator frequency tuning and control. *J. Opt. Soc. Am. B* **8**, 646 (1991).

28. S. Mosca, M. Parisi, I. Ricciardi, F. Leo, T. Hansson, M. Erkintalo, P. Maddaloni, P. De Natale, S. Wabnitz, M. De Rosa, Modulation instability induced frequency comb generation in a continuously pumped optical parametric oscillator. *Phys. Rev. Lett.* **121**, 093903 (2018).

29. D. Zhu, L. Shao, M. Yu, R. Cheng, B. Desiatov, C. J. Xin, Y. Hu, J. Holzgrafe, S. Ghosh, A. Shams-Ansari, E. Puma, N. Sinclair, C. Reimer, M. Zhang, M. Loncar, Integrated photonics on thin-film lithium niobate. *Adv. Opt. Photon.* **13**, 242–352 (2021).

30. S. Molesky, Z. Lin, A. Y. Piggott, W. Jin, J. Vuckovic, A. W. Rodriguez, Inverse design in nanophotonics. *Nat. Photonics* **12**, 659–670 (2018).

31. J. Mishra, T. P. McKenna, E. Ng, H. S. Stokowski, M. Jankowski, C. Langrock, D. Heydari, H. Mabuchi, M. M. Fejer, A. H. Safavi-Naeini, Mid-infrared nonlinear optics in thin-film lithium niobate on sapphire. *Optica* **8**, 921–924 (2021).

32. R. Becheker, M. Bailly, S. Idlahcen, T. Godin, B. Gerard, H. Delahaye, G. Granger, S. Fevrier, A. Grisard, E. Lallier, A. Hideur, Optical parametric generation in OP-GaAs waveguides pumped by a femtosecond fluoride fiber laser. *Opt. Lett.* **47**, 886–889 (2022).

33. S. T. Yang, R. C. Eckardt, R. L. Byer, Power and spectral characteristics of continuous-wave parametric oscillators: The doubly to singly resonant transition. *J. Opt. Soc. Am. B* **10**, 1684–1695 (1993).

34. Y. Kobayashi, K. Torizuka, A. Marandi, R. L. Byer, R. A. McCracken, Z. Zhang, D. T. Reid, Femtosecond optical parametric oscillator frequency combs. *J. Optics* **17**, 094010 (2015).